

COSMIC X-RAY BACKGROUND AND EARTH ALBEDO SPECTRA WITH *SWIFT* BAT

M. AJELLO,¹ J. GREINER,¹ G. SATO,² D. R. WILLIS,¹ G. KANBACH,¹ A. W. STRONG,¹
 R. DIEHL,¹ G. HASINGER,¹ N. GEHRELS,² C. B. MARKWARDT,² AND J. TUELLER²

Received 2008 April 2; accepted 2008 August 16

ABSTRACT

We use *Swift* BAT Earth occultation data at different geomagnetic latitudes to derive a sensitive measurement of the cosmic X-ray background (CXB) and of the Earth albedo emission in the 15–200 keV band. We compare our CXB spectrum with recent (*INTEGRAL*, *BeppoSAX*) and past results (*HEAO-1*) and find good agreement. Using an independent measurement of the CXB spectrum we are able to confirm our results. This study shows that the BAT CXB spectrum has a normalization $\sim 8\% \pm 3\%$ larger than the *HEAO-1* measurement. The BAT accurate Earth albedo spectrum can be used to predict the level of photon background for satellites in low Earth and mid inclination orbits.

Subject headings: cosmology: observations — diffuse radiation — Earth — galaxies: active —
 X-rays: diffuse background

Online material: color figures

1. INTRODUCTION

There is a general consensus that the cosmic X-ray background (CXB), discovered more than 40 years ago (Giacconi et al. 1962), is produced by integrated emission of extragalactic point sources. The deepest X-ray surveys to date (Giacconi et al. 2002; Alexander et al. 2003; Hasinger 2004) have shown that up to virtually 100% of the < 2 keV CXB radiation is accounted for by active galactic nuclei (AGNs) hosting accreting supermassive black holes (SMBHs). However, the fraction of CXB emission resolved into AGNs declines with energy being $< 50\%$ above 6 keV (Worsley et al. 2005). The unresolved component may be attributed to the emission of a yet undetected population of highly absorbed AGNs. These AGNs should be characterized by having column densities $\sim 10^{24}$ H atoms cm^{-2} and a space density peaking at redshift below 1 (Worsley et al. 2005). Such a population of Compton-thick AGNs is invoked by population synthesis models (e.g., Comastri et al. 1995; Treister & Urry 2005; Gilli et al. 2007) to reproduce the peak of the CXB emission at 30 keV (Marshall et al. 1980).

Thus, an accurate measurement of the CXB spectrum in the 15–200 keV energy range is important to assess and constrain the number density of Compton-thick AGNs. Such measurements are complicated by the fact that instruments sensitive in this energy range are dominated by internal detector background and are not designed to measure the CXB spectrum directly (excluding *HEAO-1* A2). The typical approach is to produce an ON – OFF measurement, where taking the difference between the ON and the OFF pointings eliminates the internal background component.

There are different methods to obtain a suitable OFF observation; the *HEAO-1* measurement of the CXB spectrum in the 13–180 keV range was obtained by blocking the aperture with a movable CsI crystal. Also the Earth disk can be used to modulate the CXB emission. This approach is the one used in recent CXB intensity measurements performed by *INTEGRAL* and *BeppoSAX* (Churazov et al. 2007; Frontera et al. 2007).

Here we report on two independent measurements of the CXB emission using *Swift* BAT. For the first method, we use the Earth occultation technique similarly to the *INTEGRAL* and *BeppoSAX* analyses while for the second one we make use of the spatial distribution of the BAT background.

The structure of the paper is as follows. In § 2 we present the details of the observations and describe the BAT background components. We also derive a rate-rigidity relation which is fundamental for suppressing the background variability due to cosmic rays (CRs). In § 3 we present the details of the Earth’s occultation episodes undergone by BAT and the analysis method for the occultation measurement. In § 4 we discuss all sources of uncertainties which affect our occultation measurement which is then presented in § 6. The alternative measurement used to verify the results of the occultation analysis is reported in § 7. We discuss the broadband properties of the CXB and Earth spectra in § 8. Finally, the last section summarizes our findings.

2. OBSERVATIONS

The Burst Alert Telescope (BAT; Barthelmy et al. 2005), aboard the *Swift* mission (Gehrels et al. 2004), launched by NASA in 2004, represents a major improvement in sensitivity for X-ray imaging of the hard X-ray sky. BAT is a coded mask telescope with a wide field of view (FOV; $120^\circ \times 90^\circ$ partially coded) sensitive in the hard X-ray domain (15–200 keV). BAT’s main purpose is to locate and to study gamma-ray bursts (GRBs). While chasing new GRBs, BAT surveys the hard X-ray sky with an unprecedented sensitivity. Thanks to its wide FOV and its pointing strategy, BAT monitors continuously a large fraction of the sky (up to 80%) every day.

The *Swift* satellite constraints require that the pointing direction be at least 30° above the Earth’s horizon. Nevertheless, due to its extent, it may happen that the Earth disk occults a substantial portion (up to 30%) of the BAT FOV. Moreover, BAT survey data include episodes of large occultation (up to $\sim 70\%$) caused by the Earth when the spacecraft was in “safe” mode.

We use 8 months of BAT data which constitutes a well characterized data set of BAT survey data (see Ajello et al. 2008a, 2008b for details) to study the different components of the BAT background. Our first aim is to derive the BAT background spectrum in the infinite-rigidity approximation. We then use all

¹ Max-Planck-Institut für Extraterrestrische Physik, Postfach 1312, 85741, Garching, Germany.

² Astrophysics Science Division, Mail Code 661, NASA Goddard Space Flight Center, Greenbelt, MD 20771, USA.

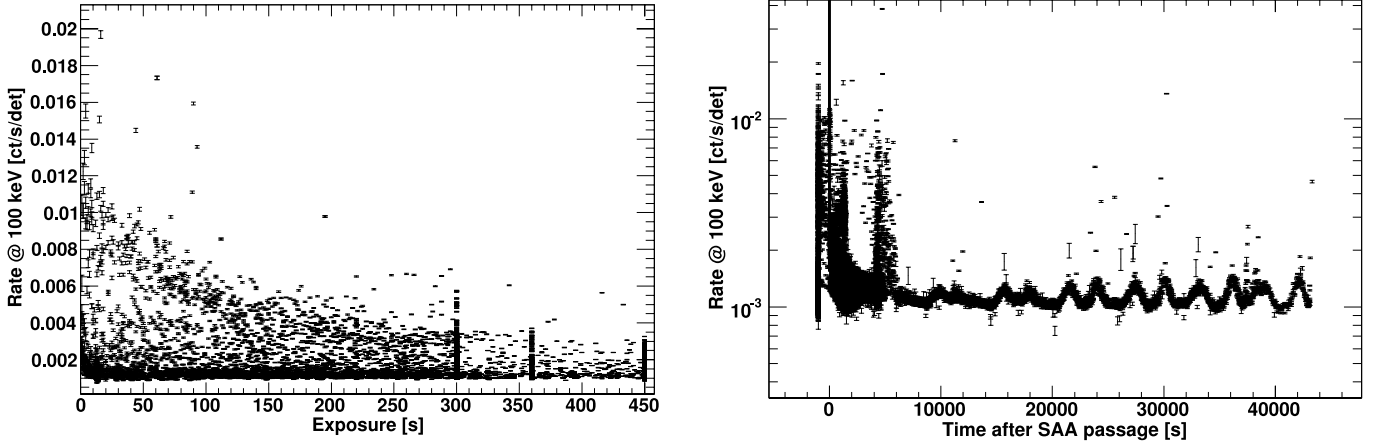


FIG. 1.—*Left*: BAT rate at 100 keV vs. exposure time. The “truncated” exposures below 300 s are noisy. Despite the impression most ($\geq 90\%$) of the observations have exposure larger than (or equal) 300 s. *Right*: BAT rate at 100 keV vs. time after each SAA passage. Note the sharp increase in rate and decay behavior when the spacecraft exits the SAA. The second sharp peak at ~ 4000 s is due to a subsequent passage within the tail of the SAA. The rate modulation visible after ~ 6000 s is due to the Earth’s magnetosphere. Negative times are used for exposure taken within the SAA.

occultation episodes, as described in § 3, to derive a measurement of the CXB and the Earth atmosphere spectra.

2.1. The BAT Background

The BAT background is highly complex and structured; it exhibits variability dependent on both orbital position and pointing direction. BAT employs a graded-Z fringe shield to suppress the in-orbit background. The fringe shield, located around and below the BAT detector plane, reduces the isotropic cosmic diffuse flux and the anisotropic Earth albedo by $\sim 95\%$ (Barthelmy et al. 2005). The two main background components are the CXB emission and the cosmic-ray-induced (prompt and delayed) backgrounds.

The CXB spectrum in the 3–400 keV range is derived from *HEAO-1* data. The following analytical approximation was suggested by Gruber et al. (1999):

$$S_{\text{CXB}}(E) = 7.877E^{-0.29}e^{-E/41.13} \quad \text{for } 3 < E < 60 \text{ keV},$$

$$S_{\text{CXB}}(E) = 0.0259\left(\frac{E}{60}\right)^{-5.5} + 0.504\left(\frac{E}{60}\right)^{-1.58} + 0.0288\left(\frac{E}{60}\right)^{-1.05}, \quad \text{for } E > 60 \text{ keV}, \quad (1)$$

where $S_{\text{CXB}}(E)$ is expressed in units of $\text{keV cm}^{-2} \text{s}^{-1} \text{sr}^{-1} \text{keV}^{-1}$. Given the large FOV (~ 1.4 sr half-coded), the CXB is the dominant background component in BAT up to ~ 50 – 60 keV.

The prompt CR background is due to spallation effects of incident CRs on the material of the spacecraft; since the Earth magnetic field modulates the flux of incident CRs across the orbit, such background component is expected to vary with the cutoff rigidity R_c (i.e., the minimum momentum an incident charged particle must have in order to penetrate into the Earth’s magnetosphere). The delayed component is caused by the excitation of the materials from the incident CR flux. This component builds up on times short compared to the relevant decay lifetimes, then varies as the slower of the irradiation or the lifetime. The Earth’s magnetic field includes an indentation in the southern hemisphere called the South Atlantic Anomaly (SAA). During each SAA passage, BAT experiences a sharp increase in count rate due to the increase of the incident CR flux and a delayed background due to de-excitation of the spacecraft materials.

In order to discriminate the various components of the BAT background, we correlated the BAT whole array rate (in each energy channel and normalized by the number of working detectors) with several orbital parameters. The final goal is to derive a “steady state” BAT background model which is unaffected by orbital variations.

2.1.1. Data Selections

Our aim is to determine a rate-rigidity relation in order to extrapolate the BAT array rates to the infinite-rigidity case; this allows us to model the background variability due to the prompt and delayed CR components.

First we selected the data excluding all observations where sources with signal-to-noise ratio (S/N) greater than 8 are detected. An 8σ source produces an increase in rate of less than 0.5% in a typical 300 s observation³; thus all pointlike sources below this limit give a negligible contribution to the background level.

The next step is to eliminate all observations whose exposure time is less than 300 s. As Figure 1 (*left panel*) shows, for exposures below 300 s, the rates show a clear anticorrelation with exposure time, with an increase of a factor ~ 3 in the rates for few seconds of exposures. Exposures below 300 s are usually the result of a truncated observation because (1) BAT detects a GRB or (2) BAT enters in the SAA and data acquisition is suspended. For any of these reasons, data of truncated exposures are excluded by the present analysis because they are not representative of the average BAT background.

Whenever the spacecraft exits the SAA, BAT experiences a rate decline due to de-excitation of spacecraft materials. As shown in Figure 1 (*right panel*) the rates reach their normal level after ~ 5600 s after each SAA passage. By excluding all observations taken within ~ 5600 s of an SAA passage, we thus eliminate short-lived radioactivity effects.

The BAT rates also show a correlation with the angle between the Sun and the pointing direction. This correlation becomes visible at angles $> 120^\circ$ and decreases with energy, disappearing at 70–80 keV. The reason of this rate increase with the angle to the Sun is unclear. However, since the number of these observations is small ($\sim 5\%$), we decided to exclude them from the present analysis.

³ BAT survey observation have typically an exposure of 300 s, although shorter and longer exposures might exist.

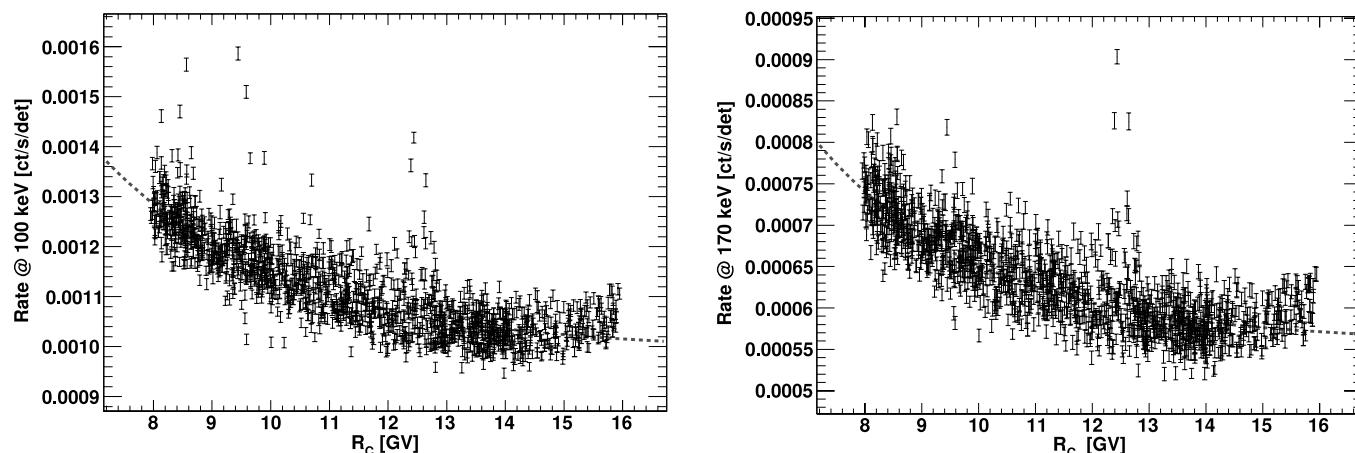


FIG. 2.—*Left*: Correlation of BAT rate with the cutoff rigidity at 100 keV. The dashed line is the best fit using an exponential plus a constant. Only those observations which passed the selection criteria explained in § 2.1.1 were used. *Right*: Correlation of BAT rate with the cutoff rigidity at 170 keV. The dashed line is a exponential plus a constant fit. The outliers present in both figures around 12 GV are due to the spacecraft being in the vicinity of the SAA. Only those observations which passed the selection criteria explained in § 2.1.1 were used. [See the electronic edition of the Journal for a color version of this figure.]

The BAT effective area declines with energy and at ~ 200 keV reduces to 1/5 of its peak value at 50 keV; moreover, at these energies the fringe shield becomes partially transparent. Thus, it is possible to use the high-energy channels as a “particle” detector to monitor the background level of the instrument (i.e., these channels do not yield much information on any celestial signal). We found that imposing that the rate of the last energy channel (194 keV–6.5 MeV) be in the range 10–20 counts s^{-1} eliminates roughly 1% of the observations which are outliers in all the correlations we have studied.

After these cuts, we find, as expected, that the rates in each energy channel decrease as a function of the cutoff rigidity R_c . This effect is shown for two representative energy channels in Figure 2. We model this behavior with an exponential and a constant (rate = $C + Be^{\alpha R_c}$), and fit this model to each energy channel. The fitted constant C provides an estimate of the BAT rate in the infinite-rigidity extrapolation. The distribution of the steepness of the rate increase with rigidity (α -values), shown in left panel of Figure 3, has a mean of -0.34 and a rms of 0.04 , in perfect agreement with previous measurements (Imhof et al. 1976).

The BAT spectrum obtained by extrapolating the rates of each energy channel to infinite rigidity is shown in the right panel of Figure 3. The bumpiness between 60 and 100 keV is due to the

numerous fluorescence emission lines from the fringe shield (see Willis 2002 for details).

3. EARTH OCCULTATION

The *Swift* orbital constraints require that the BAT pointing direction be always at least 30° away from the Earth horizon. This is because the Earth is bright in optical and X-rays, thus it may damage the UV/Optical telescope (UVOT) and the X-ray telescope (XRT). On 2005 May 31, June 12, and July 28, the *Swift* spacecraft entered into “safe” mode because of star tracker loss of lock. In safe-mode operations, the XRT and UVOT telescopes are closed, but BAT still takes data. The spacecraft remains in Sun reference pointing until commanding from the ground recovers *Swift* back to its normal status. In the time span between the safe mode and the recovering operation, the satellite uses the magnetometers and the Sun sensor to derive its pointing direction. At least in the occasions mentioned above⁴ the Earth passed through the BAT field of view (FOV). Figure 4 shows the BAT pointing directions during the deep occultation episodes described here.

⁴ A few episodes of Earth occultation were found in BAT data, but some did not pass the criteria explained in § 2.1.1.

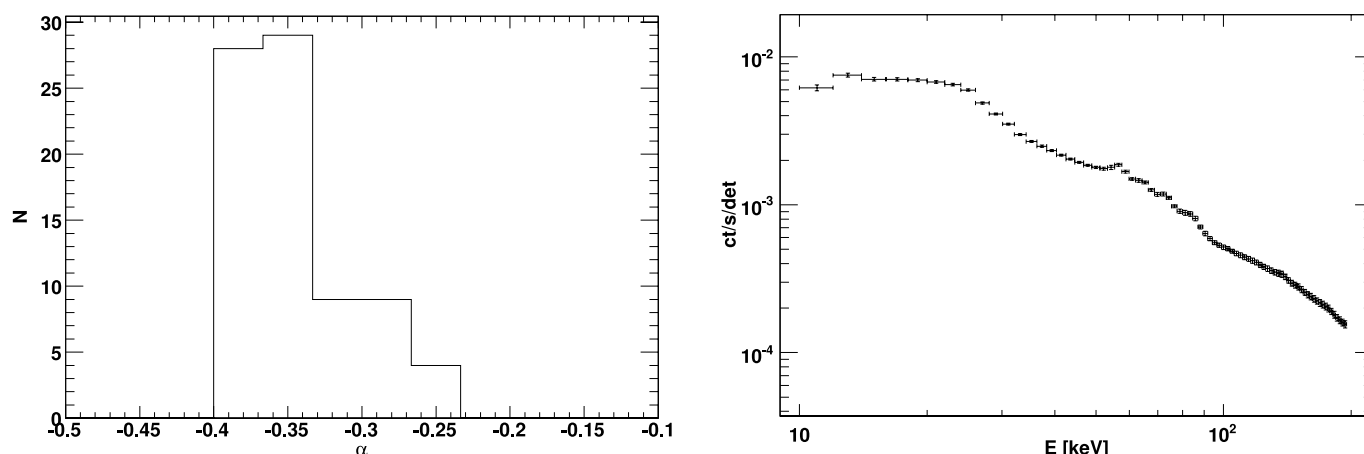


FIG. 3.—*Left*: Distribution of the α -values. The mean of -0.34 is in good agreement with measurements from Imhof et al. (1976). *Right*: BAT background spectrum extrapolated in the infinite rigidity case.

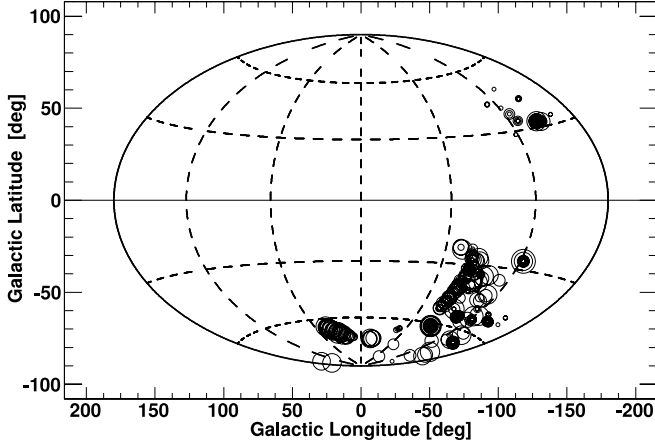


FIG. 4.—Pointing directions for the occulted observations. Marker sizes vary linearly with the occulted FOV fraction. Occultations vary from 0.1% to ~80%. In order to avoid contamination of the CXB signal from the Galactic Ridge emission, we used only occultation episodes at $|b| > 20^\circ$ (data points already excised from this plot).

As the Earth partially occults the FOV, BAT registers a sharp decrease in rate due to occultation of the CXB emission. This is especially evident below 40 keV where the CXB radiation dominates above the Earth's atmospheric components. The left panel of Figure 5 clearly shows the drop in rates caused by the occulting Earth; between 18–20 keV the rates drop by a factor 3.5 when ~60% of the BAT FOV is occulted (as shown in the right panel of Fig. 5).

Thus, the Earth occultation can be used to measure the CXB emission by means of the depression caused in the BAT rates. Unfortunately, the Earth is not only a passive occulter, but also an active emitter. The Earth is a powerful source of X- and gamma rays due to cosmic-ray bombardment of its atmosphere (see Petry 2005; Sazonov et al. 2007). This radiation is usually referred to as albedo, and it is discussed briefly in the next section.

3.1. Atmospheric Albedo Gamma Rays

The atmospheric albedo flux is produced by cosmic-ray interactions in the Earth's atmosphere. Hadronic interaction with atmospheric nuclei of the incident cosmic rays leads to the production

of an electromagnetic and nuclear cascade with muons, nuclear fragments, and other hadrons. Gamma rays above 50 MeV are produced mainly by the decay of mesons, while at X-ray energies the main source can be attributed to bremsstrahlung from secondary electrons.

Measurements of the X-ray albedo radiation are reported in Schwartz & Peterson (1974) in the 1–100 keV energy range and by Imhof et al. (1976) above 40 keV. The albedo spectrum measured by Schwartz & Peterson (1974) shows a cutoff below 30 keV, probably due to self-absorption of the radiation emitted from the inner layers of the atmosphere and a progressive flattening around 40 keV. Above 40 keV the albedo emission decreases as a power law with photon index of ~ 1.4 – 1.7 . This power-law behavior is confirmed by other experiments (e.g., Schönfelder et al. 1980; Gehrels 1992) and by a recent Monte Carlo simulation of the hard X-ray emission of the Earth's atmosphere (Sazonov et al. 2007). However, the absolute normalization of the observed Earth spectrum depends on the altitude and the inclination of the satellite's orbit and on the solar cycle.

3.2. Method of Analysis

The rate $R(E)_i$ measured at energy E by BAT in a given observation, during which the Earth is in the FOV, can be described as

$$R(E)_i = I(E)_i - \bar{\Omega}_i [R(E)_{\text{CXB},i} - R(E)_{\text{Earth},i}], \quad (2)$$

where the subscript i refers to the i th observation, $\bar{\Omega}_i$ is the “effective” solid angle occulted by the Earth, $I(E)$ is the total background, and $R(E)_{\text{CXB}}$ and $R(E)_{\text{Earth}}$ are the CXB and the Earth emission respectively.

The observations we are dealing with are generally noncontiguous, and thus all changes in the instrument configuration (e.g., number of working detectors) must be taken into account. We do this by computing the “effective” solid angle occulted by the Earth for each observation. This is defined as

$$\bar{\Omega}_i = \sum_{j=0}^{N_p} \omega_j (1 - \Delta T_j^{\text{frac}}) V_j^i, \quad (3)$$

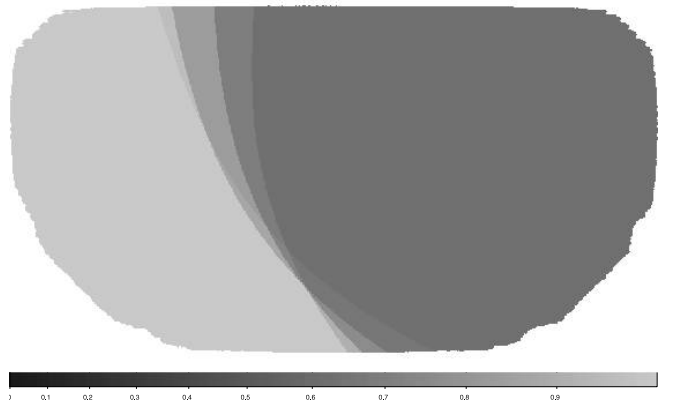
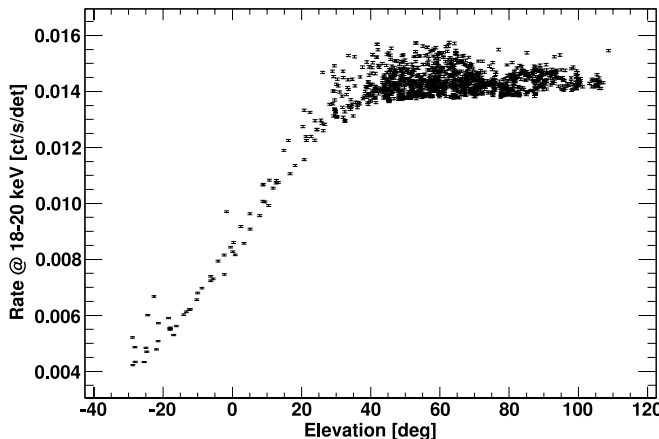


FIG. 5.—*Left*: BAT rate, in the 18–20 keV range, as a function of the elevation angle above the Earth horizon. For FOV $< 30^\circ$ – 60° , BAT starts to experience Earth occultations. The decrease in rate is expected to vary linearly with the occulted solid angle if Earth emission is negligible. Note that this graph is not a light curve as each data point is a separate (in time) 300 s observation. *Right*: Example of deep Earth occultation of the BAT FOV. The black area is the region of the BAT FOV which is completely occulted by the Earth during the 300 s observation; the lighter gray is the unocculted part of the FOV, while the region in between the black and the lighter gray is partially occulted due to the spacecraft movement in the 300 s. The color bar shows the fractional time a given sky pixel is unocculted.

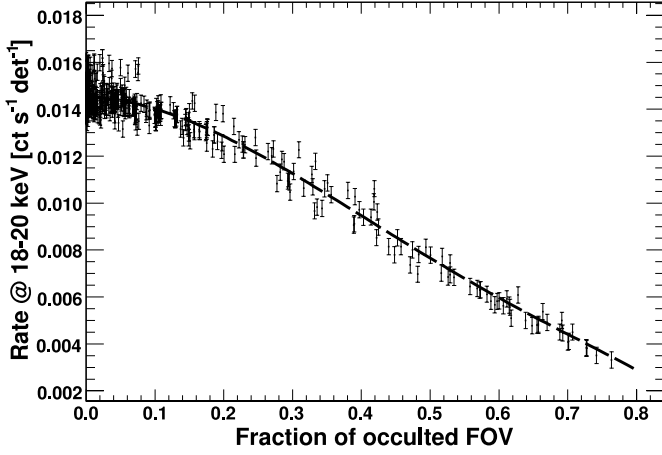


FIG. 6.—Fit example for the 18–20 keV energy channel. The long dashed line is the best fit to the data. Note that the occultation of the CXB emission produces a very strong signal reducing the background rate by $\sim 75\%$.

where N_p is the total number of sky pixels, ΔT_j^{frac} is the fractional exposure time⁵ a sky pixel of solid angle ω_j is unocculted, and V_j^i is the vignetting affecting that sky pixel during the i th observation.

Equation (2) shows the “degeneracy” problem which limits the Earth occultation technique when used to determine the CXB emission. Indeed, the measured depression of the rates with respect to the normal sky intensity level are a measurement of the difference of the CXB intensity and the Earth’s atmospheric emission. Following the notation of equation (2), this can be expressed as $R(E)_i = R(E)_{\text{CXB},i} - R(E)_{\text{Earth},i}$. We adopt here an approach similar to the one of Churazov et al. (2007) and Frontera et al. (2007) which consists of deriving the “difference” (ON – OFF) spectrum and fitting it with a priori spectral models.

The difference spectrum is derived fitting equation (2) to each energy channel (an example is shown in Fig. 6). In all these independent fits the two parameters $[I(E)_i$ and $R(E)]$ are left unconstrained. Moreover, in order to avoid contamination by the Galactic Ridge emission we used only occultation episodes at Galactic latitude larger than 20° . The difference spectrum is shown in Figure 7. However, before describing the spectral fit we discuss in detail the sources of systematic uncertainties affecting our analysis.

3.2.1. A Note on the “Degeneracy” Problem

The “degeneracy” problem (i.e., the fact that the CXB and the albedo emissions leave a similar signature during the occultation of the BAT FOV) might in principle be alleviated modeling the albedo emission of the Earth. This involves modeling the emission as a function of the cutoff rigidity of the visible disk as well as the (reasonably) expected nonuniformity of the albedo emission (i.e., limb or disk brightening effects).

Indeed, since the albedo emission is generated at different cutoff rigidities, with respect to the local rigidity of the satellite, one might reasonably expect that patches of the disk located at lower cutoff rigidities emit a larger X-ray flux. This information might be used to disentangle the albedo from the CXB signal. Moreover, the Earth is known to be a nonuniform emitter at MeV and GeV energies. Both COMPTEL and EGRET (Schönfelder et al. 1980; Petry 2005) have shown that the Earth exhibits a bright

⁵ The fractional exposure time is the fraction of the exposure time the sky pixel is unocculted. Thus, it varies from 0 to 1 for completely occulted and unocculted pixels respectively.

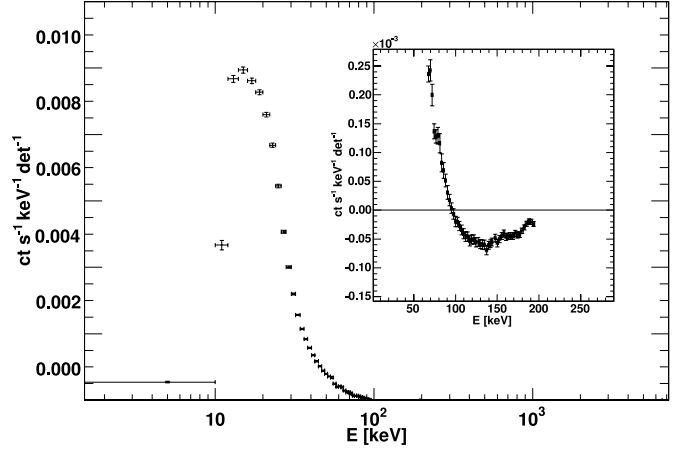


FIG. 7.—ON – OFF difference spectrum obtained fitting eq. (2) to each energy channel as shown in Fig. 6. The inset shows the negative part of the spectrum. Above 100 keV the albedo spectrum dominates the CXB emission.

limb. Thus, also this information might be used to model the expected emission.

However, we note that a few factors limit the application, in this analysis, of the modeling described above. The limitations come from the fact that this analysis is entirely based on survey data. As explained in § 2.1.1, the typical integration time for the survey is 300 s. Thus, we do not have a time-resolved monitoring (e.g., 1 s time resolution) of the transit of the Earth across the BAT FOV, but only 300 s snapshot observations with different level of occultations. Moreover, since the Earth is moving in the FOV within these 300 s, all the physical quantities (e.g., cutoff rigidity, fraction of the occulted FOV, etc.) are necessarily averaged over this time. Another limitation is due to the fact that the observations used here are not contiguous in time, but separated by weeks or months. Thus, the changing background conditions limit the precision of this analysis (as also shown in § 4.1).

These facts limit the usage of a precise modeling of the Earth albedo emission which would allow to disentangle the albedo and the CXB signal without assuming a priori spectral templates. A dedicated Earth observation with BAT in “burst” mode (i.e., event-by-event mode) would not only allow to overcome the problems shown above, but also would extend the energy range of the measurement up to 350 keV (instead of 200 keV) and would also reduce the systematic uncertainties of the measurement to those related to the instrumental response only (see § 4).

4. ANALYSIS OF THE UNCERTAINTIES

4.1. Rate Variation

The rate-rigidity graphs (examples are shown in Fig. 2) show a scatter in the rate around the best fit, which is generally larger than the statistical errors. This scatter is due to unknown effects. The pointing directions, the solar cycle, the spacecraft orientation with respect to the Earth and the Sun could be at the origin of this scatter which has an amplitude of less than 10%. We modeled the scatters as a Gaussian distribution such that the 1σ width of this distribution gives for each energy channel an estimate of the total (statistical plus systematic) error of the extrapolated rates. This constitutes the baseline uncertainty of this analysis, and it is propagated throughout all the further steps.

4.2. Uncertainties Connected to Imprecise Attitude Determination

During safe-mode operations, attitude determination relies on the magnetometers and Sun sensor. The derived attitude solution

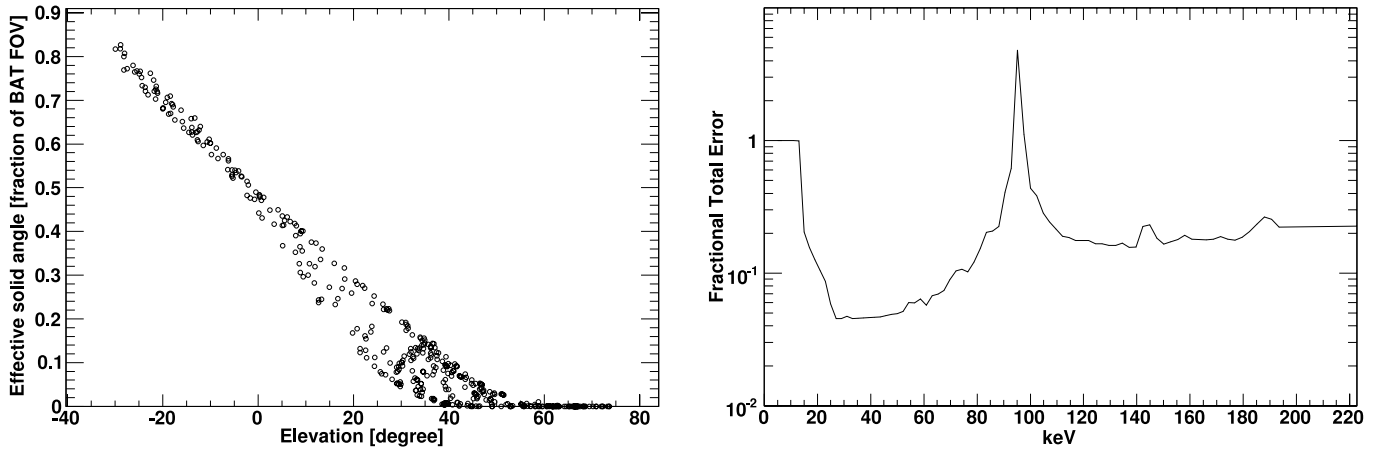


FIG. 8.—*Left*: Variation of the fractional effective solid angle as a function of elevation (distance of the pointing direction with respect the Earth limb). *Right*: Fractional 1σ total uncertainty as a function of energy. The fractional uncertainty includes all the error estimates outlined in § 4. The total error reaches its minimum of 4%–5% at the peak of the CXB emission. The peak around 100 keV is artificial and corresponds to the change of sign of the difference spectrum. Uncertainties above 100 keV are $\sim 20\%$ and primarily systematic in origin.

has a precision of the order of $\sim 1^\circ$. This is confirmed by the analysis of sources detected during safe-mode pointings, which shows that the attitude differs from the nominal pointing direction by 1° – 2° . The effective solid angle, computed in equation (3), is a slowly varying function per degree of occultation. As shown in the right panel of Figure 8, the fractional effective solid angle can be approximated by a straight line with a slope of 0.010 deg^{-1} in the 0.4–0.8 range of fractional occulted FOV. This means that an error of (at most) 2° in the attitude determination translates into an uncertainty of $\sim 2\%$ in the determination of the occulted portion of BAT FOV. This additional systematic uncertainty is taken into account in our analysis.

4.3. Uncertainties of the BAT Instrumental Response

The BAT is a well-calibrated instrument. However, given the very large FOV and the uncertainty in the modeling of spacecraft materials, the Crab Nebula is detected with slightly different spectral parameters across the FOV. To cope with this uncertainty, users are encouraged, when performing spectral fitting, to use a vector of energy-dependent systematic errors⁶ which allows a unique spectral fit to the Crab Nebula wherever in the FOV. In this analysis, we account for such systematic errors, which fortunately have their minimum ($\sim 4\%$) in the 20–80 keV band.

5. INSTRUMENTAL RESPONSE TO A DIFFUSE SOURCE

The BAT response was developed by characterizing individual CdZnTe detector pixels, and by modeling the absorption and modulation of the coded aperture mask, then finally verifying by Monte Carlo simulations with radio active sources (Sato et al. 2005). However, since there remained uncertainty in response to continuum emissions, the response was adjusted to fit the Crab nebula spectrum.⁴ The BAT Crab spectrum can be described as $dN/dE = 10.40 E^{-2.14}$ photons $\text{cm}^{-2} \text{s}^{-1} \text{keV}^{-1}$. The values of normalization and photon index are well within those used by most of the X-ray missions in a similar band (see Kirsch et al. 2005 for a review of Crab Nebula spectral parameters).

However, the analysis of a diffuse source (as the CXB) presents some differences with respect to the study of point-like objects. Indeed, the spectrum of a pointlike source is modulated by the coded mask pattern. Thus, the indirect unmodulated component

which is scattered by the materials of the BAT instrument and of the satellite can be eliminated. Accordingly, the official response generator, *batdrngen*, part of the standard BAT software, produces a response only for the direct component. However, the CXB, the subject of this paper, is seen as a diffuse emission and cannot be modulated by the coded mask pattern. We therefore utilized the Monte Carlo simulator to generate a more accurate response for a diffuse emission taking into account the scattered component,⁷ as well as the effect of isotropic illumination of the BAT instrument. This simulator is the one used to verify the response on the ground, but the same corrections to fit the Crab spectrum are also applied.

6. RESULTS OF THE ANALYSIS

In this section we present the main results of the analysis: the CXB and the Earth’s atmosphere spectra. All the uncertainties described in § 4 were added in quadrature to form the total uncertainty. The dependence of the total uncertainty with energy is shown in Figure 8 (*right*). The total uncertainty reaches its minimum value of 4–5% at the peak of the CXB spectrum.

In this section all quoted errors on spectral parameters are 90% confidence for one interesting parameter.

6.1. Spectral Fitting

The ON – OFF difference spectrum is folded in XSPEC (Arnaud 1996) with the proper instrumental response for a diffuse source. The model we used for the fit is the difference between the CXB and the albedo spectra. For the CXB spectrum we employ equation (1). For the albedo spectrum we use a jointly smoothed double power law of the form:

$$\frac{dN}{dE} = \frac{C}{(E/E_b)^{\Gamma_1} + (E/E_b)^{\Gamma_2}} \quad (\text{photons cm}^{-2} \text{s}^{-1} \text{sr}^{-1}), \quad (4)$$

where Γ_1 and Γ_2 are the two spectral indices and E_b is the break energy. This functional form reproduces well the atmospheric component with its decline at low energy, bump around 30–40 keV, and a hard spectral index at higher energies (Schwartz &

⁶ A detailed discussion is reported in http://swift.gsfc.nasa.gov/docs/swift/analysis/bat_digest.html.

⁷ The so-called uncoded (or scattered) component comprises all those events which scatter in the satellite structure and produce a detectable signal in the BAT array.

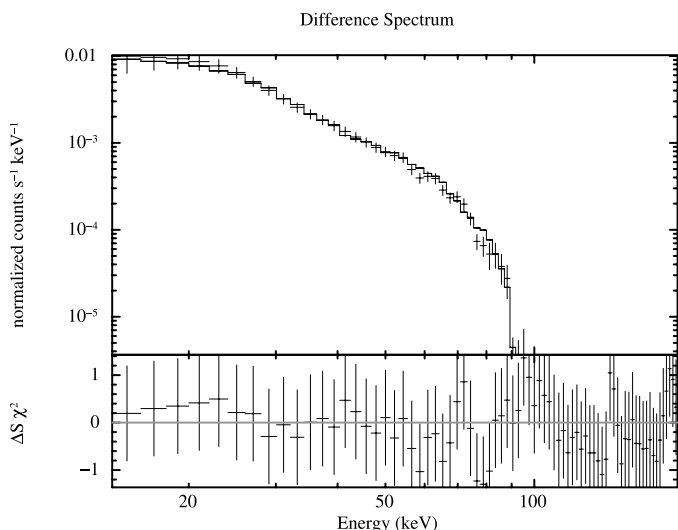


FIG. 9.—Best fit to the ON – OFF difference spectrum. The model used is the difference between eqs. (1) and (4). Around 100 keV, the data become negative (as shown in Fig. 7). [See the electronic edition of the *Journal* for a color version of this figure.]

Peterson 1974; Imhof et al. 1976; Gehrels 1985; Frontera et al. 2007). Recent Monte Carlo simulations of the Earth emission (Sazonov et al. 2007) show that equation (4) is a very good approximation of the Earth emission below 300 keV. We fix the values of the spectral indices and break energy at those suggested by Sazonov et al. (2007) i.e., $\Gamma_1 = -5$ and $\Gamma_2 = 1.4$ and $E_b = 44$ keV. Thus, free parameters of our first fit are only the normalizations of equations (1) and (4), respectively. The fit is poor, however, with a χ^2 of ~ 220 for 75 degrees of freedom. Adding free parameters for the high-energy spectral index Γ_2 and the break energy E_b improves the fit ($\chi^2_{\text{red}} = 121.8/73$). The F -test confirms that the improvement is very significant (F -test probability of 4.8×10^{-10}). Adding another free parameter for the low energy spectral index Γ_1 of the albedo does not improve the fit. Indeed, below 40 keV the spectrum is completely dominated by the CXB emission, and thus it is not possible to constrain this parameter. Choosing as free variables the parameters

of the Earth emission instead of those of the CXB spectrum is well motivated: there are indications (Schwartz 1969; Gehrels 1985; Frontera et al. 2007) that the high-energy spectral index of the albedo emission might be steeper than the classical value of 1.4. On the other side, the formula shown in equation (1) (Gruber et al. 1999) is a good representation of the broadband CXB spectrum.

Our best-fit parameters (with 90% CL errors) for the albedo spectrum are: $\Gamma_2 = 1.72 \pm 0.08$, $E_b = 33.7 \pm 3.5$ keV and $C = 1.48^{+0.6}_{-0.3} \times 10^{-2}$. The normalization, and its 90% CL error, of the CXB as measured by BAT with respect equation (1) is 1.06 ± 0.08 . This error includes also the change by ± 1 in the low-energy spectral index (Γ_1) of the albedo emission. The CXB intensity in the 20–50 keV band is $6.43 (\pm 0.20) \times 10^{-8}$ ergs cm $^{-2}$ s $^{-1}$ sr $^{-1}$. Figure 9 shows the best fit and its residuals to the difference spectrum.

7. ALTERNATIVE MEASUREMENT OF THE X-RAY BACKGROUND SPECTRUM

The BAT in-flight background has a peculiar spatial distribution which shows larger count rates toward the center of the detector array and smaller rates toward its edges. This is clearly shown in Figure 10 (*left*). In the process of forming sky images, the BAT software⁸ removes this background component by means of an empirical bidimensional second-order polynomial function.

This feature has an important physical meaning. Indeed, it is the result of a diffuse isotropic source (namely the CXB), shining through the mask. The peculiar shape of this “background” component arises from the fact that detectors at the edge of the array have a smaller solid angle of the sky as seen through the mask (they see the mask under large angles) than those at the very center. Given the extent of the BAT mask and array, this effect is noticeable and significant.

We thus built a simple model, assigning to each detector its geometrical solid angle through the transparent mask elements. This model is shown in Figure 10. We can detect the CXB emission by

⁸ For reference see the description of the `batclean` tool available at <http://heasarc.nasa.gov/lheasoft/ftools/headas/batclean.html>.

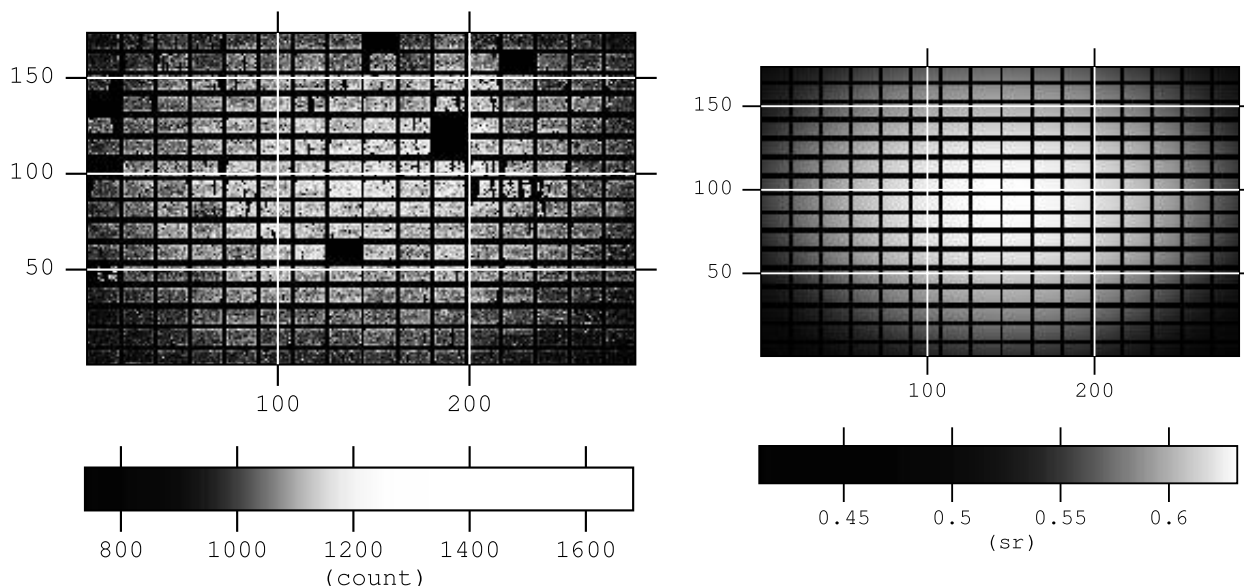


FIG. 10.—*Left*: BAT detector plane image in the 15–55 keV energy channel. *Right*: Model of the detectors solid angles distribution. The similarity of the model with the real data (*left*) is apparent.

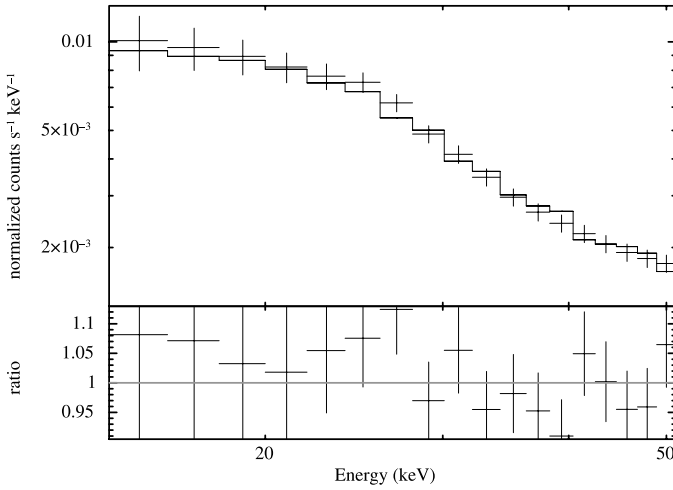


FIG. 11.—Best fit to the second CXB measurement using eq. (1) with only the overall normalization left as free parameter. [See the electronic edition of the *Journal* for a color version of this figure.]

fitting this model to the spatial distribution of the counts in each energy channel. However, this approach is valid only as long as the graded-Z shield remains opaque to X-ray photons (~ 50 keV). Indeed, as soon as the shield becomes partially transparent, the effective detector solid angle increases because of the shield transparency. Thus, our model becomes inadequate above this energy.

7.1. Model Fitting

Among all BAT observations which satisfied the selection criteria outlined in § 2.1.1, we selected only those ones which were unocculted by the Earth. We then summed all the detector plane histograms⁹ (DPHs) into a single DPH with an overall exposure of ~ 1.8 Ms. Summing the DPHs of observations with different pointing directions achieves the goal of smearing the contribution of sources which are below the detection threshold (8σ in this case). To each energy channel we fitted a model which is composed of

1. a constant term for the edges of the detector modules which register a higher count rate because of the larger exposed area;
2. the solid angle distribution model which takes into account the diffuse flux as seen through the mask;
3. a constant term which takes into account all other background components including the CR component which penetrates through the shielding.

For each energy channel, the fit independently determines the intensity of the diffuse model. Since all the energy-dependent effects (e.g., absorption through the mask structure and transparency of the lead tiles) are correctly taken care of in the instrumental response described in § 5, we normalize our model (dividing by the maximum detector solid angle ~ 0.6 sr) and treat the dispersion of the solid angle distribution (~ 0.034 sr) as a fluctuation. In this way, we make our approach insensitive to the exact computation of the solid angle for each detector and at the same time, it allows us to use the same response matrix developed for the occultation measurement. We remark that this response matrix is based on extensive Monte Carlo simulations.

7.2. Results

For spectral fitting we convolved the CXB count rate spectrum with the BAT response matrix. For each energy channel, we

⁹ BAT survey data are in the form of 80 channels detector plane histograms with a typical exposure time of 300 s.

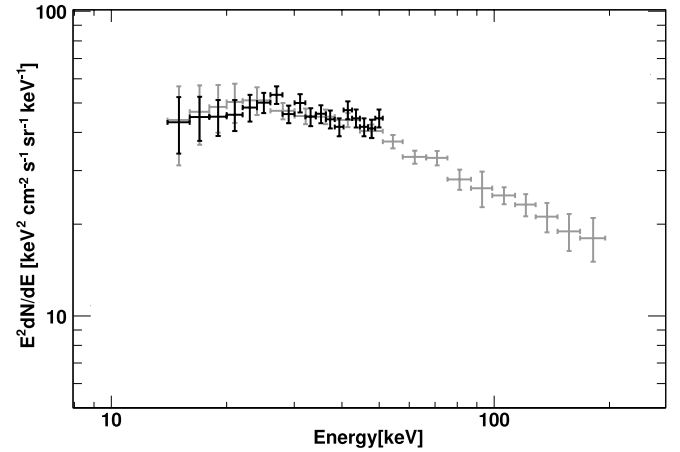


FIG. 12.—Two independent measurements of the CXB spectrum performed by BAT. The occultation measurement (gray data points) and the measurement derived using the solid angle distribution (black data points) are in very good agreement.

summed in quadrature statistical uncertainty, the uncertainty on the mean solid angle (see § 7.1) and the uncertainty due to the BAT response (see § 5).

A fit to the data allowing only the overall CXB normalization (eq. [1]) to vary yields a χ^2 of 18.8 for 17 degree of freedom. The best fit and residuals are shown in Figure 11. The normalization with respect to the level of the CXB as measured by Gruber et al. (1999) is $1.09^{+0.03}_{-0.03}$. This measurement is in very good agreement with the occultation measurement as Figure 12 shows.

8. COMPARISON WITH PREVIOUS MEASUREMENTS

In this section we compare the CXB and the albedo spectra with previously available measurements in the same or overlapping energy bands. For reference, the values of CXB and albedo emissions as derived by BAT are reported in Table 1.

8.1. The X-Ray Background Spectrum

Both measurements of the CXB spectrum presented here produce the same results (within errors) for the normalization of the CXB intensity at its peak. Combining both measurements we determine that the CXB intensity at its peak is $8\% \pm 3\%$ larger than previously measured by *HEAO-1* (Gruber et al. 1999). We find that the CXB intensity in the 20–50 keV band is $(6.50 \pm 0.15) \times 10^{-8}$ ergs $\text{cm}^{-2} \text{s}^{-1} \text{sr}^{-1}$. The observed intensity near the peak of the CXB spectrum (expressed in νF_ν units) at 30 keV is $46.2 \text{ keV}^2 \text{cm}^{-2} \text{s}^{-1} \text{keV}^{-1} \text{sr}^{-1}$. Figure 13 shows the comparison of the BAT CXB spectrum with all other measurements available above 20 keV. All measurements agree well within 10%. The detailed comparison is reported in Table 2. It is clear that the scatter in CXB intensities does not depend solely on the adopted spectra for the Crab Nebula. Some of the measurements showed in Table 2 might still be affected by systematic uncertainty in the instrumental response used. To our knowledge, BAT is the only instrument for which a dedicated instrumental response has been derived and tested for the analysis of the CXB.

Figure 14 shows a compilation of the X- and gamma-ray diffuse backgrounds from keV to GeV energies. In addition to the work of Gruber et al. (1999) we show *SMM* (Solar Maximum Mission) (MeV) data (Watanabe et al. 1997), and COMPTEL and EGRET data in a recent revision (Weidenspointner et al. 2000; Strong et al. 2004). In particular, the new analysis of EGRET data shows that the validity range of the Gruber et al. (1999) formula (eq. [1]) is now restricted to $3 \text{ keV} < E < 1 \text{ MeV}$.

TABLE 1
COSMIC X-RAY BACKGROUND AND ALBEDO EMISSION INTENSITIES

Energy (keV)	ΔE	CXB (keV ² cm ⁻² s ⁻¹ sr ⁻¹ keV ⁻¹)	CXB 1 σ Error	Albedo ^a (10 ⁻⁴ photons cm ⁻² s ⁻¹ sr ⁻¹ keV ⁻¹)	Albedo 1 σ Error
15.0.....	2.0	43.92	12.71
17.0.....	2.0	46.82	10.35
19.0.....	2.0	48.58	8.65
21.0.....	2.0	50.39	7.42
24.0.....	4.0	50.96	5.28
28.1.....	4.1	47.12	2.90
32.2.....	4.1	45.26	2.72	63.96	19.36
36.2.....	4.1	45.07	2.52	73.93	13.75
41.4.....	6.3	44.00	2.34	76.25	9.50
47.8.....	6.5	40.39	2.07	74.94	6.32
54.3.....	6.5	37.33	1.89	64.57	4.72
62.0.....	8.8	33.25	1.63	55.01	3.29
70.9.....	9.0	32.99	1.79	38.30	2.85
81.2.....	11.6	28.08	2.17	34.16	3.14
92.9.....	11.8	26.25	3.50	26.53	4.00
106.1.....	14.5	24.86	1.61	20.64	1.36
120.8.....	15.0	23.18	1.93	16.41	1.37
137.2.....	17.9	21.15	2.32	13.43	1.46
156.8.....	21.2	18.95	2.62	10.96	1.43
181.1.....	27.5	18.02	2.96	8.38	1.22

^a In the 14–30 keV energy range the 1 σ upper limit to the albedo intensity is 6.3×10^{-3} photons cm⁻² s⁻¹ sr⁻¹ keV⁻¹.

We find that a good description of the available data in the 2 keV–2 MeV range is achieved using a smoothly joined double power law of the form

$$E^2 \frac{dN}{dE} = E^2 \times \frac{C}{(E/E_B)^{\Gamma_1} + (E/E_B)^{\Gamma_2}} \quad (\text{keV}^2 \text{ photons cm}^{-2} \text{ s}^{-1} \text{ sr}^{-1} \text{ keV}^{-1}) \quad (5)$$

The best fit, shown in Figure 14, yields values (and 1 σ errors) of: $C = (10.15 \pm 0.80) \times 10^{-2}$, $\Gamma_1 = 1.32 \pm 0.018$, $\Gamma_2 = 2.88 \pm 0.015$, and $E_B = 29.99 \pm 1.1$ keV. The reduced χ^2 is acceptable (~ 1.2) considering the number (10) of different data sets fitted. The suggested formula reproduces well the CXB spectrum over

two decades in flux and five in energy. At a given energy, the systematic uncertainty produced by the scatter of the measurements used here is of the order of 10%.

Note that, there is no astrophysical need to connect the keV and the GeV diffuse backgrounds with a single formula (e.g., Gruber et al. 1999). It is generally agreed that the source populations contributing to the two diffuse backgrounds are probably different. Almost all of the CXB radiation up to 300 keV can be explained in terms of emission-line AGNs (e.g., Gilli et al. 2007). Moreover, taking into account (the likely, but not yet detected) population of nonthermal electrons in AGN coronae, Inoue et al. (2008) successfully reproduce the CXB emission up to 4 MeV. On the other hand, blazars account only for $\leq 25\%$ of the GeV diffuse background and most likely other source classes contribute to the diffuse emission (Dermer 2007).

TABLE 2
COMPARISON WITH PREVIOUS RESULTS

Instrument	Reference	Energy Band (keV)	F_{Crab}^a	I_{CXB}^b
HEAO-1 A2+A4	1	20–50	9.92 ^c	6.06 ± 0.06
HEAO-1 A2	2	20–50	NA	5.60 ± 0.30
BeppoSAX	3	20–50	9.22	5.89 ± 0.19
INTEGRAL	4	20–50	10.4	$\sim 6.66^d$
BAT	5	20–50	9.42 ^c	6.50 ± 0.15

^a Crab flux quoted by the authors expressed in 10^{-9} ergs cm⁻² s⁻¹ keV⁻¹.

^b Intensity of the CXB quoted by the authors in 10^{-8} keV² cm⁻² s⁻¹ sr⁻¹ keV⁻¹.

^c Gruber et al. (1999) do not report about their adopted Crab spectrum; however the HEAO-A4 spectrum of the Crab Nebula can be described (below 57 keV) as $dN/dE = 8.76 E^{-2.0.75}$ photons cm⁻² s⁻¹ keV⁻¹ (Jung 1989).

^d Authors do not give an exact measurement of the CXB flux, but report that their measurement is $\sim 10\%$ higher than the Gruber et al. (1999) spectrum.

^e The value quoted here has to be taken as a reference value. The systematic uncertainties discussed in § 4.3 allow to derive consistent Crab Nebula fluxes across the entire BAT FOV.

REFERENCES.—(1) Gruber et al. 1999; (2) Marshall et al. 1980; (3) Frontera et al. 2007; (4) Churazov et al. 2007; (5) this work.

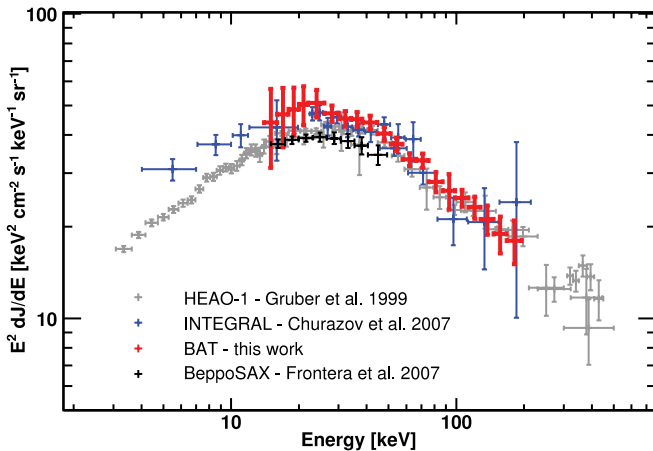


FIG. 13.—Comparison of CXB measurements above 20 keV. The BAT spectrum (red) is in agreement with the HEAO-1 (gray), INTEGRAL (blue) and BeppoSAX (black) observations. For clarity only the BAT occultation measurement is reported.

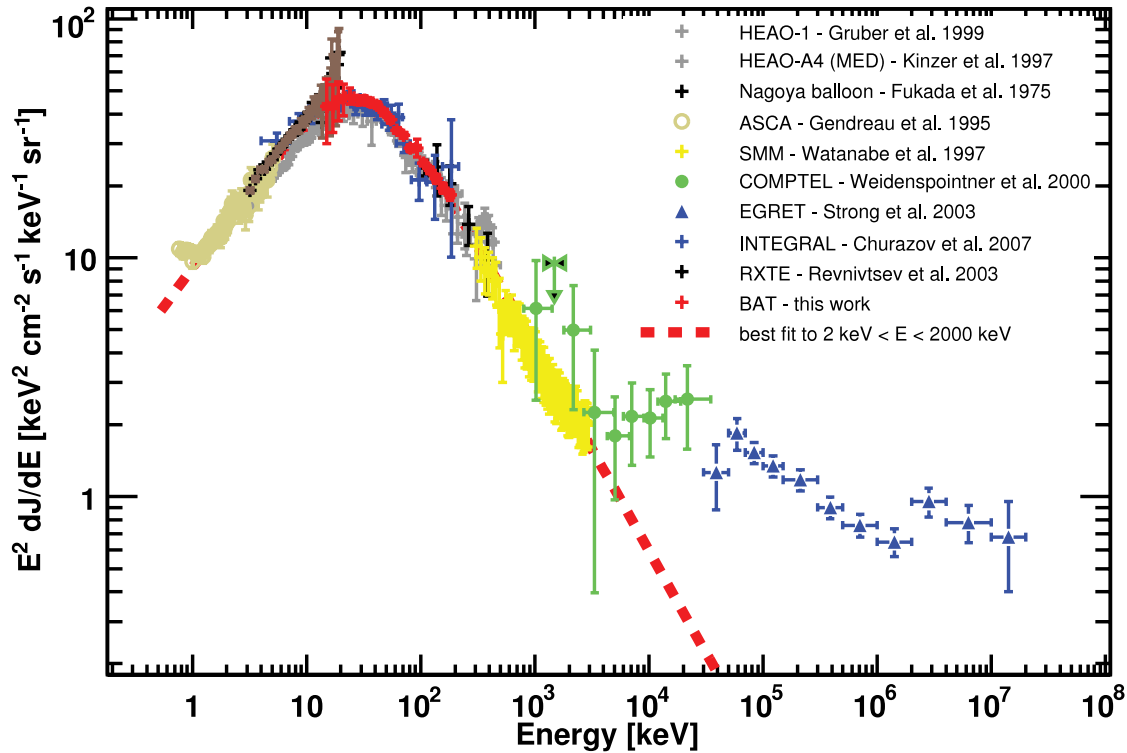


FIG. 14.—BAT CXB spectrum compared with previous results. The dashed line is the best fit to $2 \text{ keV} < E < 2000 \text{ keV}$, as reported in the text.

8.2. The Earth Albedo Spectrum

Our Earth albedo spectrum is not compatible with the classical high-energy photon index of 1.4. The BAT data are consistent with a steeper high-energy photon index at 99.989 confidence level.

Using the polar-orbiting satellite *1972-076B*, Imhof et al. (1976) found that above 40 keV the photon spectrum is consistent with a power law with an index ranging from 1.34 to 1.4, depending on the latitude range scanned. Their measurement is based on the difference between pointings toward the atmosphere (down) and pointing toward the sky (up). In order to derive the albedo spectrum, the authors sum the CXB emission and the down-up spectrum (see eq. [5] in Imhof et al. 1976 for details). For the CXB emission, they adopt the measurement of Pal (1973) which de-

scribes the CXB photon spectrum as $dN/dE = 25E^{-2.1}$. This representation differs from the *HEAO-1* CXB spectrum in both normalization and photon index in the 40–200 keV range. Thus, we adjusted the Imhof et al. (1976) albedo spectra, taking into account the differences between the Gruber et al. (1999) and the Pal (1973) CXB spectral representations. This is shown in Figure 15. After the correction, the two (equatorial and polar) albedo spectra are consistent with a power law with photon index ~ 1.7 . In particular the equatorial measurement is in good agreement with the BAT spectrum.

The *BeppoSAX* satellite operated in a Low-Earth Orbit similar to *Swift*, but with different inclination (4°). The BAT Earth albedo

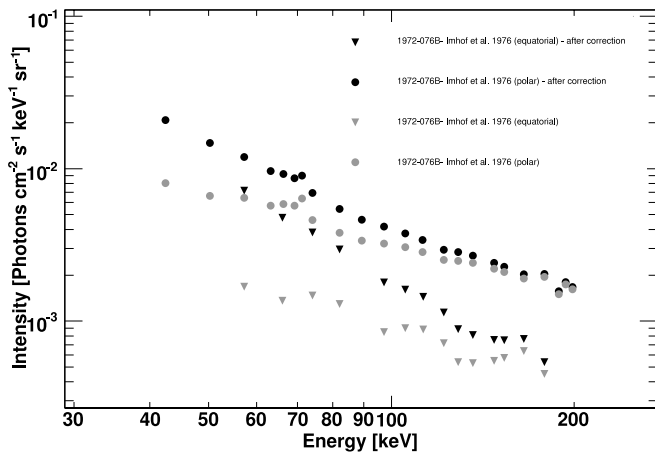


FIG. 15.—Measurements of the Earth albedo of Imhof et al. (1976) at different geomagnetic latitudes. The original measurements (gray) have been corrected for unsubtracted CXB emission (see the text for details). After the correction, the albedo spectra (black data points) become steeper.

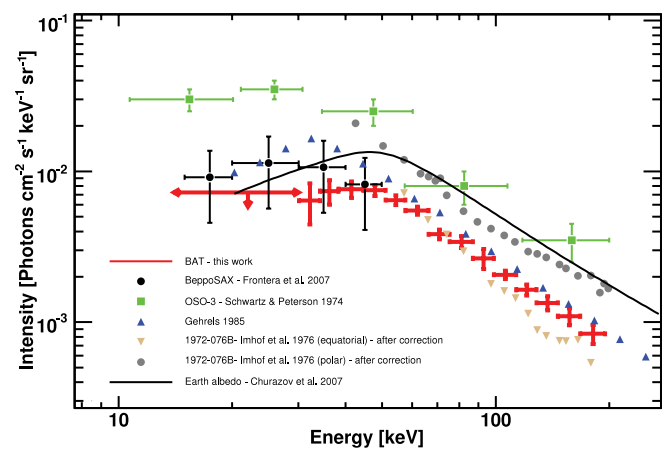


FIG. 16.—BAT Earth spectrum as compared to past measurements. References are shown in the legend. The data points (triangles) from Gehrels (1985) are a fit to the *downward* gamma-ray flux at 5 g cm^{-2} over Palestine, Texas. The measurements from Imhof et al. (1976) were corrected to take into account the correct CXB emission (details are in the text). The thin solid line shows the prediction of the Earth emission as observed from the orbit of the *INTEGRAL* satellite (Sazonov et al. 2007; Churazov et al. 2007).

spectrum is compatible (within the large uncertainties of the *BeppoSAX* analysis) with the measurements obtained by Frontera et al. (2007). It is worth noting that we derived the Earth intensity using different orbital positions (as done for *BeppoSAX* and *OSO-3*), and thus averaging over the magnetic latitude sampled by *Swift*. Moreover, as generally the Earth enters the FOV at large angles, we do not observe the upward albedo, but rather the albedo emerging at large zenith angles. This also seems confirmed by the similarity of our spectrum with the *downward* gamma-ray flux measured for a balloon over Palestine, Texas (Gehrels 1985).

Figure 16 reports also the prediction of the Earth albedo emission as observed from the orbit of the *INTEGRAL* satellite (Sazonov et al. 2007). Its normalization has been derived during the measurement of the CXB intensity (Churazov et al. 2007). It is evident that this prediction and the BAT measurement agree well in shape but not so in normalization. Among many factors, the overall normalization depends strongly on the geomagnetic latitude and the distance to the Earth. The agreement of the BAT and *INTEGRAL* albedo spectra, respectively, with the equatorial and polar measurements of Imhof et al. (1976) seem to confirm this interpretation.

9. DISCUSSION

We have used Earth occultation episodes to derive with *Swift* BAT an accurate measurement of the CXB emission in the 15–200 keV energy range. Moreover, we have proven by means of an independent technique the accuracy of the occultation analysis and of our results. The observed BAT intensity near the peak of the CXB spectrum at 30 keV is $46.2 \text{ keV}^2 \text{ cm}^{-2} \text{ s}^{-1} \text{ sr}^{-1} \text{ keV}^{-1}$ and its uncertainty¹⁰ is $\sim 3\%$ (including all systematics). The normalization of the BAT CXB spectrum at 30 keV is $\sim 8\%$ larger than the *HEAO-1* (Gruber et al. 1999) measurement and consistent with the *INTEGRAL* one (Churazov et al. 2007). Moreover, considering that the precision of the *HEAO-1* measurement at the CXB peak is 10% (Marshall et al. 1980) and that *BeppoSAX* data are compatible with a larger (up to 20%) normalization of the CXB spectrum shows that all measurements above 10 keV are consistent within their systematic uncertainties.

Such consistency is not observed at lower energies (e.g., see discussion in Revnivtsev et al. 2005). The origin of this inconsistency is unclear. However, it seems that neither cosmic variance (Barcons et al. 2000) nor differences in the flux scale calibration of each individual instrument (Revnivtsev et al. 2005; Frontera et al. 2007) may account for it. A likely reason for the discrepancy of CXB measurement in the 2–10 keV band might reside in a systematic error in the response function used for diffuse sources (Frontera et al. 2007). To our knowledge, BAT is the only instrument (beside *HEAO-1* A2, which was designed with the purpose of measuring the CXB) which makes use of a dedicated instrumental response developed for this particular analysis. We also note that a recent measurement of the CXB performed, in the 2–7 keV, by *Swift* XRT (Moretti et al. 2008) seems to confirm the results of *XMM-Newton* (De Luca & Molendi 2004), *RXTE* (Revnivtsev et al. 2005) and *Chandra* (Hickox & Markevitch 2006). If confirmed, this means that the CXB spectrum, as most recently measured, is 25–40% larger (with respect the measurement of *HEAO-1*) below 10 keV, but only $\sim 10\%$ larger above 20 keV. The functional form we provide in § 8.1 for the broad-band CXB emission approximates well this scenario.

A larger than previously estimated CXB emission would in turn require a larger density of Compton-thick AGNs both in the local and in the more distant universe. Recently, *Chandra* stack-

ing analyses of mid-IR selected sources unveiled a large population of Compton-thick AGNs at high redshift (Daddi et al. 2007; Fiore et al. 2008). This large fraction of Compton-thick AGNs found at $z \sim 2$ can be accommodated if the emitted (obscured) flux is very low. Indeed, lowering the assumed scattering efficiency (ratio of reflected to nuclear flux) would increase by the same amount the number of Compton-thick AGNs at any redshift. In this framework, the recent discoveries of Compton-thick AGNs with an extremely low scattering efficiency (Ueda et al. 2007; Comastri et al. 2007) fits well. These AGNs are likely buried in a geometrically thick torus that obscures most of the nuclear flux. Although there can be many of these hidden AGNs, their individual contribution to the CXB is necessarily small. This seems to be confirmed by the fact that the contribution of the mid-IR selected, $z \sim 2$, AGNs is $< 3\%$ of the CXB intensity in the 10–30 keV band (Daddi et al. 2007). Therefore, a larger contribution should be provided by Compton-thick AGNs at lower redshift.

10. CONCLUSIONS

BAT performed a very sensitive measurement of the CXB emission in the 15–200 keV energy range. This measurement takes advantage of several episodes of CXB flux modulation due to Earth's passages through the BAT FOV. We find that the BAT CXB spectrum is in good agreement with the *INTEGRAL* one and that its normalization is $\sim 8\%$ larger than the *HEAO-1* measurement at 30 keV. In addition, performing an independent measurement of the CXB in the 15–50 keV band, we are able to confirm this result. Remarkably, our study also shows that all the available measurements in the > 10 keV range agree within their systematic uncertainties. The new analyses of COMPTEL and EGRET data (Weidenspointner et al. 2000; Strong et al. 2004) show that the formula suggested by Gruber et al. (1999) for the diffuse X- and gamma-ray backgrounds is only valid below 2 MeV. We derived a simple functional form which, in the 2–2000 keV range, approximate well (to a precision of 10%) the CXB spectrum.

Our study also derives the Earth albedo spectrum averaged over the magnetic latitudes sampled by *Swift*. The BAT spectrum is in agreement with all the previous observations performed by satellites operating in similar LEO orbits. This work shows that the Earth albedo spectrum declines at energies > 40 keV according to a power law with photon index of ~ 1.7 , and not as 1.4 as previously thought. A reanalysis of the measurements performed by Imhof et al. (1976) is in perfect agreement with the BAT Earth albedo spectrum. The good agreement among the available measurements allows to use the BAT Earth albedo spectrum to predict the background contribution from the Earth for other instruments operating at similar orbits.

We are grateful to S. Barthelmy, J. Cummings and H. Krimm for all the effort spent in keeping the BAT perfectly operating. M. A. acknowledges the useful suggestions of R. Mushotzky and the help of C. Gordon for adapting XSPEC to the purposes of this analysis. The anonymous referee is acknowledged for his/her helpful comments which improved the manuscript. M. A. is grateful to S. Sazonov and A. Zoglauer for interesting discussions about the Earth emission. This research has made use of data obtained from the High Energy Astrophysics Science Archive Research Center (HEASARC) provided by NASA's Goddard Space Flight Center. M. A. acknowledges funding from the DFG Leibniz-Prize to G. H. (HA 1850/28-1).

¹⁰ Derived combining both measurements of the CXB.

REFERENCES

- Ajello, M., Greiner, J., Kanbach, G., Rau, A., Strong, A. W., & Kennea, J. A. 2008a, *ApJ*, 678, 102
- Ajello, M., et al. 2008b, *ApJ*, 673, 96
- Alexander, D. M., et al. 2003, *AJ*, 126, 539
- Arnaud, K. A. 1996, in *ASP Conf. Ser. 01, Astronomical Data Analysis Software and Systems V*, ed. G. H. Jacoby & J. Barnes (San Francisco: ASP), 17
- Barcons, X., Mateos, S., & Ceballos, M. T. 2000, *MNRAS*, 316, L13
- Barthelmy, S. D., et al. 2005, *Space Sci. Rev.*, 120, 143
- Churazov, E., et al. 2007, *A&A*, 467, 529
- Comastri, A., Gilli, R., Vignali, C., Matt, G., Fiore, F., & Iwasawa, K. 2007, *Prog. Theor. Phys. Suppl.*, 169, 274
- Comastri, A., Setti, G., Zamorani, G., & Hasinger, G. 1995, *A&A*, 296, 1
- Daddi, E., et al. 2007, *ApJ*, 670, 173
- De Luca, A., & Molendi, S. 2004, *A&A*, 419, 837
- Dermer, C. D. 2007, *ApJ*, 659, 958
- Fiore, F., et al. 2008, *ApJ*, 672, 94
- Frontera, F., et al. 2007, *ApJ*, 666, 86
- Gehrels, N. 1985, *Nucl. Instrum. Methods Phys. Res. A*, 239, 324
- . 1992, in *Nucl. Instrum. Methods Phys. Res.*, 313, 513
- Gehrels, N., et al. 2004, *ApJ*, 611, 1005
- Giacconi, R., Gursky, H., Paolini, F. R., & Rossi, B. B. 1962, *Phys. Rev. Lett.*, 9, 439
- Giacconi, R., et al. 2002, *ApJS*, 139, 369
- Gilli, R., Comastri, A., & Hasinger, G. 2007, *A&A*, 463, 79
- Gruber, D. E., Matteson, J. L., Peterson, L. E., & Jung, G. V. 1999, *ApJ*, 520, 124
- Hasinger, G. 2004, *Nucl. Phys. B Proc. Suppl.*, 132, 86
- Hickox, R. C., & Markevitch, M. 2006, *ApJ*, 645, 95
- Imhof, W. L., Nakano, G. H., & Reagan, J. B. 1976, *J. Geophys. Res.*, 81, 2835
- Inoue, Y., Totani, T., & Ueda, Y. 2008, *ApJ*, 672, L5
- Jung, G. V. 1989, *ApJ*, 338, 972
- Kirsch, M. G., et al. 2005, *Proc. SPIE*, 5898, 22
- Marshall, F. E., Boldt, E. A., Holt, S. S., Miller, R. B., Mushotzky, R. F., Rose, L. A., Rothschild, R. E., & Serlemitsos, P. J. 1980, *ApJ*, 235, 4
- Moretti et al., A. 2008, *A&A*, submitted
- Pal, Y. 1973, in *IAU Symp. 55, X- and Gamma-Ray Astronomy*, ed. H. Bradt & R. Giacconi (Dordrecht: Reidel), 279
- Petry, D. 2005, in *AIP Conf. Ser. 745, High Energy Gamma-Ray Astronomy*, ed. F. A. Aharonian, H. J. Völk, & D. Horns (Melville: AIP), 709
- Revnivtsev, M., Gilfanov, M., Jahoda, K., & Sunyaev, R. 2005, *A&A*, 444, 381
- Sato, G., et al. 2005, *Nucl. Instrum. Methods Phys. Res. A*, 541, 372
- Sazonov, S., Churazov, E., Sunyaev, R., & Revnivtsev, M. 2007, *MNRAS*, 377, 1726
- Schönfelder, V., Graml, F., & Penningsfeld, F.-P. 1980, *ApJ*, 240, 350
- Schwartz, D. A. 1969, Ph.D. thesis, Univ. California (San Diego)
- Schwartz, D. A., & Peterson, L. E. 1974, *ApJ*, 190, 297
- Strong, A. W., Moskalenko, I. V., & Reimer, O. 2004, *ApJ*, 613, 956
- Treister, E., & Urry, C. M. 2005, *ApJ*, 630, 115
- Ueda, Y., et al. 2007, *ApJ*, 664, L79
- Watanabe, K., Hartmann, D. H., Leising, M. D., The, L.-S., Share, G. H., & Kinzer, R. L. 1997, in *AIP Conf. Ser. 410, Proc. Fourth Compton Symposium*, ed. C. D. Dermer, M. S. Strickman, & J. D. Kurfess (Melville: AIP), 1223
- Weidenspointner, G., et al. 2000, in *AIP Conf. Ser. 510, American Institute of Physics Conference Series*, ed. M. L. McConnell & J. M. Ryan (Melville: AIP), 467
- Willis, D. R. 2002, Ph.D. thesis, Univ. Southampton
- Worsley, M. A., et al. 2005, *MNRAS*, 357, 1281